Assessment of the Numerical Properties of ReFRESCO: a Pressure-Based Compressible Flow Solver

Cristiano Miguel Filipe Silva
cristiano.silva@tecnico.ulisboa.pt

Instituto Superior Técnico, Universidade de Lisboa, Portugal

January 2021

Abstract

This work assesses the numerical robustness (iterative errors) and accuracy (discretization errors) of the single-phase, pressure-based compressible flow solver developed within the ReFRESCO CFD package. The objectives of the work are threefold: check the ability to reduce iterative errors to negligible levels (robustness); estimate the order of grid convergence (accuracy) for integral and local quantities of interest and compare ReFRESCO solutions with reference data available in the open literature.
Two sets of test cases are selected: three two-dimensional, subsonic, turbulent flows (zero pressure gradient flat plate flow, bump-in-channel and NACA 0012 airfoil) available at the NASA Turbulence Modeling Resource; three two-dimensional inviscid flows over a circular-arc (bump) that correspond to subsonic, transonic and supersonic conditions that have been addressed in the open literature.
Grid refinement studies have been performed for all test cases using sets of geometrically similar grids that allow a reliable estimation of the observed order of grid convergence.
The robustness of the code is demonstrated since iterative errors can be reduced to values close to machine accuracy for (almost) all test cases. Insufficiently iteratively converged solutions of the non-linear problem increase the contribution of iterative errors and leads to inconsistent estimations of the exact solution.
Observed orders of grid convergence depends on the test case, selected quantity of interest and grid refinement level. ReFRESCO results are consistent with the reference data available in the open literature, but numerical oscillations can appear at shocks and geometric discontinuities.
Keywords: Solution Verification, Pressure-based solvers, Computational Fluid Dynamics

1. Introduction

Nowadays, Computational Fluid Dynamics (CFD) is a numerical tool commonly used in industrial applications [16]. In CFD, a numerical method is developed to simulate a fluid flow behaviour in a desired application, whether it is on a combustion chamber, over a wing, and so on. The governing equations of fluid motion are a system of partial differential equations (PDE) composed by the Navier-Stokes equations, which represent the conservation laws of mass and momentum. However, due to their complexity they are only analytically solved for simple cases [1].

One discretization technique typically employed is the Finite Volume Method (FVM), which transforms the governing flow PDE into algebraic equations by dividing the domain of interest in finite volumes [12]. The choice of primary flow variables, i.e., variables that are directly computed from the PDE, further categorizes these numerical algorithms. One possible alternatives is: pressure-based solvers [11].

In pressure-based solution techniques, which were first employed in incompressible flows [13], the mass conservation equation is modified and combined with with momentum to yield an equation for pressure [12].

Computing pressure from the continuity equation has attracted many research efforts, like [2, 11] to mention a few. The reason for that is related with physical aspects that are commonly referred to in the literature by the dual role of pressure. As explained in [11], in low-speed flows, pressure acts exclusively on the velocity field to enforce mass conservation since density is constant. On the other hand, in high-Mach number flows, velocity variations are small compared to the flow's velocity magnitude, which means that pressure mainly acts on density to satisfy mass conservation. At intermediate-speed flows, pressure acts on velocity and density alike. Thus, changes in pressure are finite and relevant throughout all speeds, making this flow quantity very interesting to consider as the main variable in all-speed flow algorithms [7].

Recently, a compressible pressure-based version

of ReFRESCO was presented [5, 6]. ReFRESCO is a CFD code designed for naval and offshore applications developed by MARIN (Maritime Research Institute Netherlands), in collaboration with other organizations around the world [10]. Most common practical problems in the Naval engineering field consider fluid incompressibility since the working fluid is water. However, certain applications like slamming or sloshing may involve multi-phase flows, where compressibility effects of the gaseous phase might be relevant. Accurate capturing of such physical phenomenon is the end-goal of ReFRESCO update, which is comprised of various steps.

This article follows up on the works of [5, 6] as an assessment of the numerical properties of ReFRESCO for compressible flows aiming at expanding their evaluation in more test cases than what has been done so far. More precisely, this work will focus on the following properties: robustness, by analysing the iterative convergence and accuracy, through order of grid convergence studies in Solution Verification exercises, according with [3], to local, integral, and surface flow quantities.

In total, simulations will be carried out on two sets of benchmark test cases: three two-dimensional (2D), subsonic, turbulent flows (flow over a flat plate with zero pressure gradient, over a bump-in-channel and over the NACA0012 airfoil); three 2D inviscid flows over a circular arc (bump) in subsonic, transonic and supersonic conditions. The viscous test cases are taken from [14], while the other is commonly addressed in the literature [11, 2]. Since reference data is available in the literature for the selected cases, this article also features a code-to-code comparison with the solutions from ReFRESCO and those of other codes.

This paper is structured as followed: section 2 presents the mathematical and numerical formulations, as well as relevant information about each test case. Section 3 presents the results for the iterative convergence, order of grid convergence studies and code to code solution comparison. Finally, this article ends in section 4 with the main conclusions.

2. Implementation

2.1. Mathematical model

The mathematical problem is composed by the Navier-Stokes equations, continuity and total energy conservation principle for a single-phase, unsteady flow of a compressible fluid. Closure of the before-mentioned system is achieved considering an ideal gas working fluid.

In turbulent flows simulations, the partial differential equations are averaged with the Favre-averaged procedure, as proposed in [18] for a statistically steady flow. The resulting Reynolds-stress term are handled assuming the Boussinesq hypothesis and the eddy-viscosity is computed with the on-equation model of Spalart & Allmaras [15].

2.2. Solution procedure

Following the Finite Volume Method formulation, the differential transport equations are solved in control volumes, or cells, that divide the entire domain. On the volume integration of convective, diffusive, transient, and source terms, the Gauss' divergence theorem is applied. As a result, the fluxes of the transported quantities are approximated in one point for each unique face of the control volume through the mid-point rule. Additionally, the convection terms of all transport equations were linearized with Picard's method. As a result, 5 linear systems of equations, plus an algebraic equation for density, are obtained and solved with a segregated approach. The linearization of the convective fluxes, plus the uncoupling of the equations and the deferred corrections, build up a non-linear residual. The iterative convergence of the non-linear problem was stooped (most of the times) when the normalized residual dropped to values lower than 10^{-8} of the L_∞ norm.

2.3. Discretization schemes

Numerical schemes are required to express the face's fluxes only in terms of cell values. The diffusive fluxes were always discretized with the central-differences scheme including non-orthogonality and eccentricity corrections. Lastly, the Gauss' theorem is used to determine the gradient of dependent variables at the cell centres. Whereas, for the convective flues the numerical schemes used are:

- In the flat plate and NACA0012 test cases, the Fromm scheme with the harmonic limiter [17] was used;
- The limited QUICK [9] scheme is present in all simulations of a viscous flow over a bump;
- Four convection schemes were used in the inviscid bump test cases: CDS blended with 10% UP, fully UP, HARM and QUICK schemes.

2.4. Test Cases

2D Zero Pressure Gradient Flat Plate: Figure 1 illustrates the domains dimensions and boundary conditions for the 2D turbulent flow over a flat plate with zero pressure gradient test case taken from [14]. For this test case, unitary density was assumed. The Reynolds number, based on a reference length $L = 1m$, is $Re = 5 \times 10^6$ and the undisturbed Mach number is $Ma = 0.2$ using a reference temperature of $T_{ref} = 300K$.

Two sets of geometrically similar grids are presented in figure 2. A set of 5 Cartesian grids [14], set N, and a set of 5 orthogonal multi-block grids, set IM. Moreover, both sets have a fixed refinement

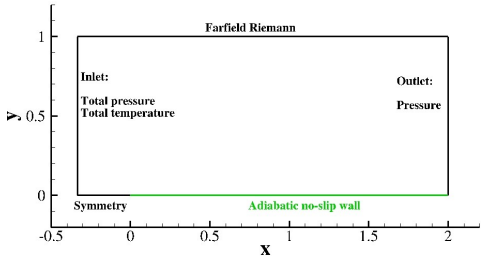

Figure 1: Domain and boundary conditions according to [14] for the calculation of the two-dimensional flow over a flat plate.

ratio of $r_i = 2$ between each consecutive grid. However, two extra grids, one between the two most refined grids and another twice as coarse, were added in both sets in order to improve the reliability of the grid convergence properties evaluation.

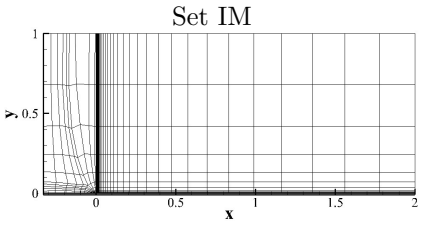

Figure 2: Illustration of the coarsest grids ($r_i = 16$) of grid sets N and IM. Two-dimensional flow over a flat plate.

2D Bump-in-channel: The viscous bump test case is another problem taken from [14]. The uniform flow's Mach number is equal to $Ma = 0.2$, based on the reference temperature $T_{ref} = 300K$, and the Reynolds number is $Re = 3 \times 10^6$, using both unitary length and density. The reference pressure is $P_{ref} = 86100Pa$. Domain dimensions along with boundary conditions are presented in figure 3. The results for this test case were obtained in only one grid set, set N, from [14], which features 5 non-uniformly spaced grids.

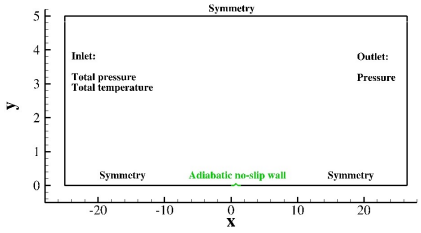

Figure 3: Domain and boundary conditions according to [14] for the calculation of the two-dimensional viscous flow over a bump.

2D NACA0012 Airfoil: The final test case of the first set is the flow around a NACA0012 airfoil. The airfoil mathematical definition was slightly modified so that its chord, c, equals to $1m$ as explained in [14], and the no-slip adiabatic wall boundary condition was applied on the surface of the airfoil. The C-shaped domain illustrated in figure 4 has the farfield Riemann boundary condition applied $500m$ away from the airfoil surface. As far as incoming flow conditions are concerned, the chord-based Reynolds equates to six million, for $\rho_{ref} = 2.1264kg/m^3$, and the undisturbed Mach number is $Ma = 0.15$, so the flow is essentially incompressible. Simulations were performed for three incoming flow angle of attack, α, 0^o, 10^o and 15^o.

Only one grid set, set N, will be used and it was taken from at [14]. It is composed of 5 grids with a fixed grid refinement ratio of 2 between each one. Figure 4 depicts the coarsest grid and a zoom around the airfoil shape. All grids share a clustering of cells at the leading and trailing edges, which is extended to the wake.

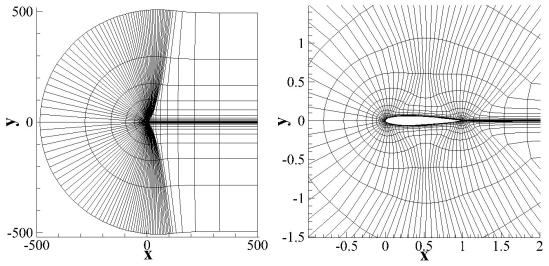

Figure 4: Illustration of the coarsest grids ($r_i = 16$) of grid set N. Two-dimensional flow over the NACA0012 airfoil.

2.5. Inviscid flow

The second set of test cases feature the 2D inviscid flow in a channel over a bump for three flow regimes: subsonic ($Ma = 0.5$), transonic ($Ma = 0.675$) and supersonic ($Ma = 1.65$). This test case is found in the open literature and it has been used to test pressure-based solvers [2, 11]. Although outside the typical speed range for maritime and offshore applications, this case was selected to test the robustness and accuracy of ReFRESCO in the presence of sharp variations of flow properties, like the Mach number in shocks. Out of the testing goal is the complex aspects of viscous flow, like shock-boundary layer interactions.

Domain's geometrical characteristics and boundary conditions depend on the incoming flow Mach number. The subsonic and transonic regimes share the same domain and boundary conditions and are depicted in the top picture of figure 5, while in the bottom illustration is clear a reduction in the bump height (from $0.1m$ to $0.04m$) for the supersonic regime, as well as, the different boundary conditions. The boundary conditions for the three test cases are also presented in 5.

Two grid sets were used for this test case. How-

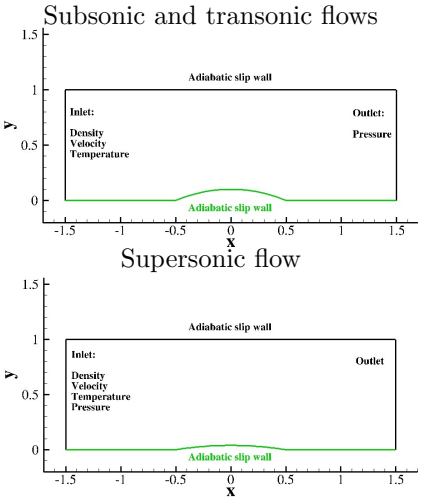

Figure 5: Domain and boundary conditions for a two-dimensional inviscid fluid flow over a circular-arc (bump).

ever, their distinction is only justified due to the geometrical variations of the bump itself since they have equal number of cells and present the same topology. For that reason, only the sparsest grid of the supersonic set is illustrated in figure 6. Each set is composed of 9 geometrically similar non-uniformly spaced Cartesian grids and the sparsest grid of each set is illustrated in figure 6. This fact, in turn, explains the need to add finer grids for the sets of this test case. However, in the supersonic test case, there were still some doubts about the extrapolations performed with data obtained from grids with $1 \leq r_i \leq 4$ and so extra grids were generated reaching a refinement level of $r_i = 0.5$. For the supersonic set, three extra grids were generated reaching a refinement level of $r_i = 0.5$. For the supersonic set, three extra grids were generated, because there were still some doubts about the extrapolations performed with data obtained from grids with $1 \leq r_i \leq 4$, reaching a refinement level of $r_i = 0.5$.

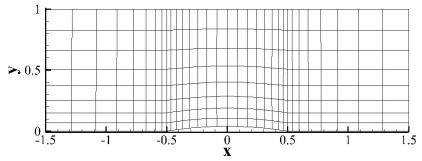

Figure 6: Illustration of the coarsest grids ($r_i = 44$) of subsonic and transonic grid set and supersonic grid set. Two-dimensional inviscid flow over a bump.

2.6. Grid convergence

One of the goals of the present study is to determine the grid convergence properties of the flow solver. The method proposed in [3] is used to estimate the numerical uncertainty of integral or local flow quantities. At least three grids are required to estimate the numerical uncertainty using least-squares fits to power series expansions.

All calculations were done in double-precision format, so the round-off error contribution to total numerical error is irrelevant. Furthermore, if the non-linear problem iterative convergence criteria is respected, the same can be assumed for the iterative error. As a result, an estimate for the discretization error ϵ_ϕ, of a flow quantity ϕ, is given from:

$$\epsilon_\phi = \phi_i - \phi_o = a h_i^p \tag{1}$$

where a is a constant, p is the observed order of grid convergence, h_i is the typical grid cell size, ϕ_i and ϕ_o are both flow quantity values in a grid with the typical cell size h_i and the estimate of the exact solution, respectively.

However, equation 1 is only suitable for a set of data obtained in the asymptotic range and monotonic behaviour are present. To improve the applicability of the error estimation process, three other error estimators are explained in [3].

The final objective of these procedures is to define the uncertainty levels of a set of data for a desired quantity. The uncertainty values are defined so that the exact solution is contained within an interval with 95% confidence. Besides considering the computed error's estimate, uncertainty values also take into account a safety factor, which accounts for the behaviour of the input data.

When presenting the results for the grid convergence studies of chosen flow quantities, the fits performed with eq. 1 are referenced by the value obtained for p with 2 significant figures, while the fixed order expressions results are identified with only 1 significant figure. Lastly, if the equation with two-terms expression in [3] represents the best fit, it will appear referenced as "$ah + bh^2$" in the legend of the plots.

By nature the results from these studies are dependent on the number of grids used and their density. To assess this dependence, four different alternatives for the estimation of observed order of grid convergence were chosen: p_a uses the data from the 5 finest grids of each set; p_b uses the solutions from the 3 finest grids using grid doubling; p_c is obtained with the data from the 4 finest grids using grid doubling; and p_d uses the solutions from 5 grids using grid doubling.

3. Results

3.1. Quantities of interest

The quantities of interest analysed for the viscous flow test cases are: skin friction coefficient C_f, pressure coefficient C_p, total drag coefficient C_D and lift coefficient C_L.

Whereas the inviscid flow over a bump test cases, the following quantities were selected: mach num-

ber Ma, stagnation temperature T_o and pressure P.

All integrals are calculated with a second-order mid point rule; and a third-order cubic interpolation is used to determine the values of C_f, C_p, Ma, T_o, and P at specific locations.

3.2. Iterative Convergence

Figure 7 depicts the L_∞ residual norm in the grid with $r_i = 4$ of the 2D bump-in-channel test case as a function of the non-linear iteration counter. The changes of dimensionless variables between two consecutive iterations are also reflected in the same plot. The simulation was run with the complete LU factorization for the linear system of the pressure-correction equation.

The noisier convergence of the energy equation is bellow the convergence criteria so it is of little concern. However, the spotlight of this analysis is on the decrease of rate of convergence with the simulation time. For example, for the figure shown, around 13 000 iterations of the non-linear system were required to drop the residuals from 10^6 to 10^7 while, from that point until the specified convergence criteria, 50 000 more were necessary. Here, the changes between each consecutive iteration are, generally, one order of magnitude higher than the residual, thus enhancing the sensitivity of the solution to the simulation time.

The origin of the degradation of the iterative rate is attributed to the fact that the near-wall cell size is replicated in the wake, where the eddy viscosity is non-zero. Diffusive effects scale with the inverse square of the cell spacing multiplied by the eddy viscosity $\left(\propto \mu_t/(\Delta {x_i}^2)\right)$, hence these terms become very large with the small near-wall distances used in this test case.

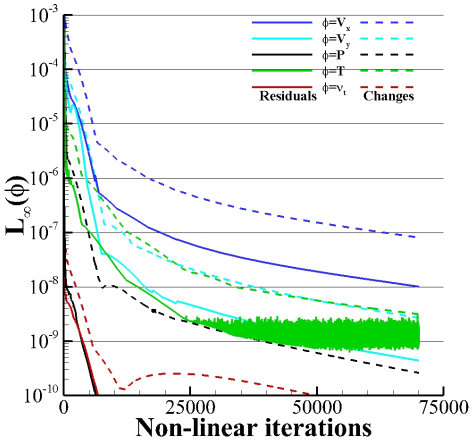

Figure 7: Illustration of the iterative convergence (L_∞ norm) in the grid with $r_i = 4.0$ of set N. Two-dimensional viscous flow over a bump.

The increasingly lower rates of convergence with respect to the residual evolution obtained for this test case motivated the following experiment: compare an insufficiently converged solution with a solution that respected the convergence criteria. More precisely, one solution was taken from a point in convergence history whereby the highest value of L_∞ norm was, approximately, 4×10^{-6}.

So, figure 8 showcases the skin friction coefficient C_f distribution along the plate+bump on the finest grid of the viscous bump test case. The red line represents the insufficiently converged solution (NConv.) and the green-coloured line the converged solution (Conv.).

It is evident that the lack of iterative convergence resulted in an overestimation of C_f. Nonetheless, to further emphasize the importance of reducing the iterative error, figure 9 presents an order of grid convergence study to C_f at $x \approx 0.63m$, using the two solutions of ReFRESCO. The estimation was performed with the data from the four finest grids, using grid doubling, and the uncertainty bars are showcased for the finest grid of the set. Only the simulation on the finest grid was insufficiently converged and the solutions on the remaining grids respected the iterative convergence criteria.

From the results in 9, it is clear the negative impact of the finest grid solution in the data set since the uncertainty bars encompass values between 5.7%, of the finest grid solution of C_f. Furthermore, the red colour fitted lines do not intersect any grid solution. The first-order grid convergence estimated for the insufficiently converged data set indicates that the estimator, which assumes a set value for "p" equal to 1 ensured the best fit to the solution of the four finest grids. This is an example where reporting of the computed order of grid convergence should be done carefully.

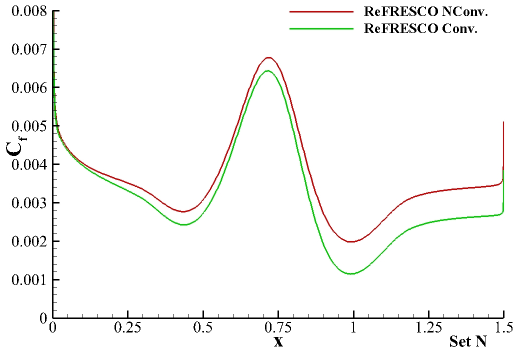

Figure 8: Skin friction coefficient C_f distribution on the finest grid of set N. Two-dimensional viscous flow over a bump.

3.3. Viscous flows test cases

3.3.1 Grid convergence studies

The results of grid convergence studies to C_D and C_f at $x = 0.970084m$ are depicted in figure 10.

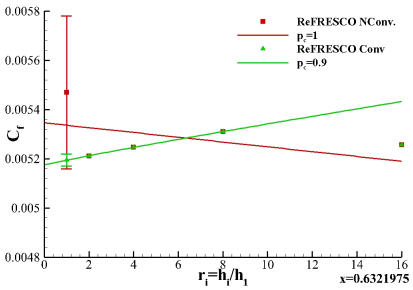

Figure 9: Grid convergence studies for the skin friction coefficient C_f at $x = 0.6321975m$. Two-dimensional viscous flow over a bump.

Both quantities were analysed in the grid sets N and IM of the flat plate test case. The lines included in the plots represent the best fit, as proposed in [3], to each discrete data set input. However, the estimated uncertainty bar corresponds only to the fit performed for the 5 finest grids (p_a).

The results for the two quantities are consistent between each grid set, which means that the uncertainty bars of the finest grids overlap. Additionally, they also showcase the deviation of the solutions obtained in coarser grids from the fitted lines based on fine grids results as the estimated order of grid convergence deteriorates if the coarsest grid $r_i = 16$ is included (p_d). Both sets extrapolate the solution for a cell size zero to, approximately, the same value if the grid with $r_i = 16$ is not included in the estimation. The error constant, a, is slightly larger for the IM set than for the set N. Lastly, while the value of p is the same between both sets when evaluating locally C_f, set IM shows lower order of grid convergence for the integral quantity C_D than set N.

Under viscous bump test case conditions, figure 11 presents three alternative estimates of p using grid doubling for C_f and C_p at 20 selected locations on the plate+bump surface. The symbols at null values of p indicate that the best fit to the data is obtained with the two terms expansion. The two plots suggest the following trends:

- The best fit for the solutions at the leading edge for C_p are obtained with the two terms expansions. Whereas, the same estimator is used for the results of C_f in the grids with $1 \leq r_i \leq 8$ at the trailing edge.
- The estimated values of p for C_f show more scatter than the ones for C_p. Not only that, but the estimated order of grid convergence is generally higher for the pressure coefficient.
- Unexpectedly, the inclusion of the coarsest grid solution does not always deteriorate the estimate of p.

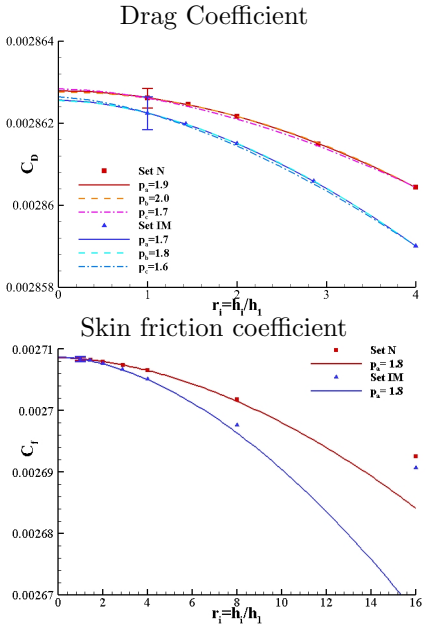

Figure 10: Grid convergence studies for C_D and C_f at $x = 0.970084m$. Two-dimensional flow over a flat plate.

3.3.2 Code-to-code comparison

Figure 12 compares the distributions of C_f for two viscous flow test cases: flow over a flat plate and over a bump. The results of ReFRESCO are compared with the solutions (available at [14]) from other flow solvers, CFL3D and FUN3D.

The differences between ReFRESCO results and the comparative data is represented in dashed lines and quantified on right-axis of figure 12. To complement the comparison, the uncertainty values computed from ReFRESCO using data from the three grids with $r_i = 1$, $r_i = 2$, and $r_i = 4$, calculated in selected points throughout the plate were also included and they too are with respect to the right-axis.

Graphically, ReFRESCO solutions are in line with other codes results. However, for the flat plate test case, the differences between ReFRESCO and the other two solvers are larger than the estimated numerical uncertainty. Generally, the disparities in the skin friction coefficient are around 4×10^{-6}, while the uncertainty levels are close to 2×10^{-7}. Nonetheless, without estimating the numerical uncertainty of the FUN3D and CFL3D solutions, there is no guarantee that the results of ReFRESCO are inconsistent. The latter was not obtained because only the distribution of C_f in the finest grid is given at [14].

While, in the viscous bump test case conditions, the highest differences are at the leading and trailing edges, which pose numerical singularities. Nonetheless, the quantification of the mismatches

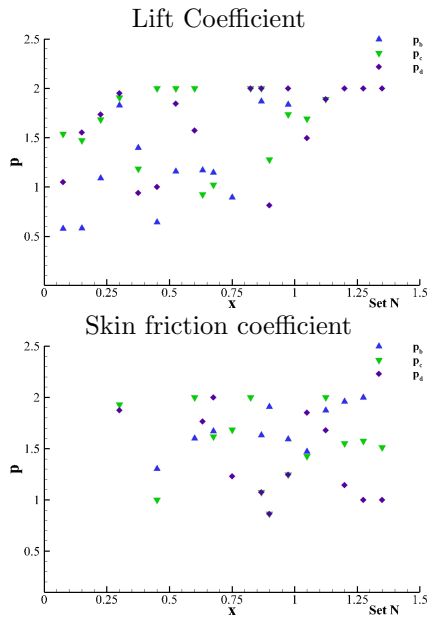

Figure 11: Estimation of p for C_f and C_p at 20 locations along the solid wall. Two-dimensional viscous flow over a bump.

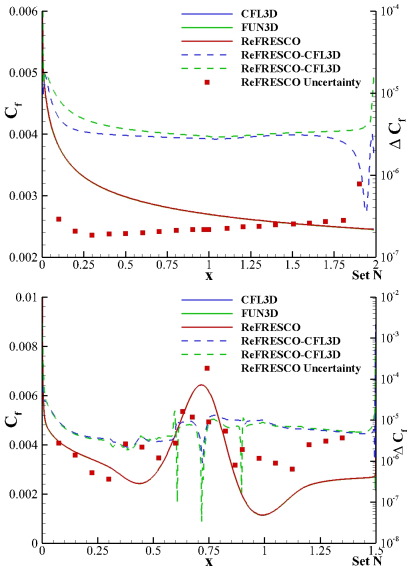

Figure 12: Skin friction coefficient C_f distribution on the finest grid of sets available at [14]. Two-dimensional flow over a flat plate (top plot). Two-dimensional viscous flow over a bump (bottom plot).

averages 5 identical digits. Furthermore, these differences correspond to the numerical uncertainties estimated for ReFRESCO along the bump. As a result, the solution from ReFRESCO is consistent with the results available in the open literature.

The results for C_f on the upper surface of the NACA0012 airfoil and pressure coefficient C_p distribution on both sides of the foil at $\alpha = 15^o$ are presented in figure 13. Besides the results from ReFRESCO, the plots also include solutions from the CFL3D solver [14] and experimental data from two sources: Ladson, et al. [8], with $Re_c = 6 \times 10^6$; and Gregory, et al. [4], with $Re_c \approx 3 \times 10^6$. The numerical solutions were obtained in second finest grid used in NACA0012 case study.

The solutions of ReFRESCO are in great agreement with the results from CFL3D flow solver for both quantities. Both codes predict a separation bubble in the upper surface of the foil at approximately $x/c = 92\%$. Similar to the trends in the viscous bump test case, the main discrepancy between ReFRESCO and CFL3D is in the numerical influences of the change in boundary conditions in the trailing edge of the foil (from no-slip solid wall to symmetry).

The experimental data reported in [4] seems to be in line to the CFD solutions despite the difference in the Reynolds number. However, the results obtained by Ladson, and co-workers [8], for $Re_c = 6 \times 10^6$ show considerable differences in the pressure peaks at the leading edge and in pressure levels across the first half of the upper surface. It is believed that these results may not sufficiently represent a two-dimensional flow because the aspect ratio of model used was only 1.333, as stated in [14].

3.4. Inviscid flow test cases

The results presented for the second set of test cases feature: Mach Ma number distributions along the bottom walls of the domain and grid convergence studies to stagnation temperature T_o and pressure P at selected locations on the bottom boundary downstream of the second geometrical singularity. The grid convergence properties are evaluated with the 4 different schemes addressed in sub-section 2.3. Additionally, the truncated power series expressions explained in 2.6 are fitted to the data of the four most refined grids, being the grids with $1 \leq r_i \leq 2.75$ for subsonic and transonic flows and grids with $0.5 \leq r_i \leq 1$ for the supersonic conditions. On the other hand, the results for the Mach number distributions will only be presented for the harmonic scheme (HARM) in grids with similar densities as the ones found in [11], i.e. the grids with $r_i = 5.5$ and $r_i = 11$.

3.4.1 Subsonic flow

The Ma distribution in figure 14 for the subsonic conditions shows little influence of the grids refinement level. As expected, the largest differences are concerned with the resolution of the geometric singularities, at the start and end of the bump, which deteriorates with grid coarsening. Nonetheless, the distributions obtained with ReFRESCO are similar

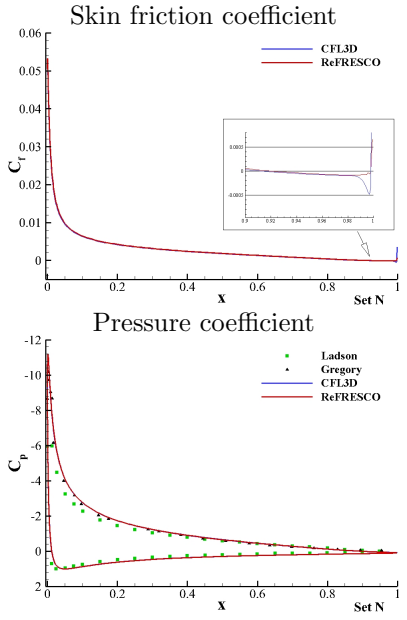

Figure 13: C_f distribution on the upper surface and C_p results around the airfoil for $\alpha = 15^o$. Two-dimensional flow over the NACA0012 airfoil.

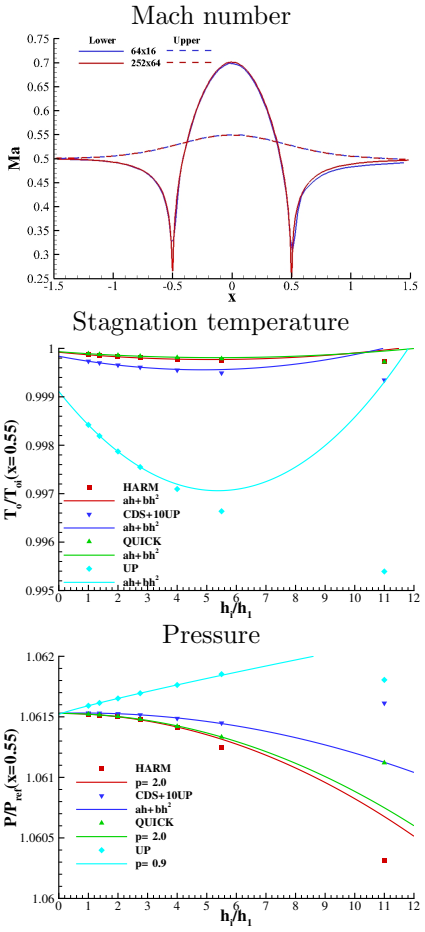

Figure 14: Mach distribution on the horizontal boundaries and grid convergence studies for stagnation temperature and pressure at $x = 0.55m$ on the lower wall. Two-dimensional subsonic inviscid flow over a bump .

to those reported in [11].

Figure 14 also presents the convergence with grid refinement for T_o and P. All schemes, but the UP scheme, extrapolate to values of T_o close to expected theoretical solution, T_o is constant for adiabatic flows of an ideal gas. However, the inconsistency of UP results is not reflected in the grid convergence of P. There, all four schemes are consistent and most of the estimated orders of grid convergence match the theoretical order of the schemes.

3.4.2 Transonic flow

Figure 15 presents the results for the Mach number distribution at the horizontal boundaries and the convergence with grid refinement for T_o and P at $x = 0.7m$ on the lower boundary for the transonic conditions.

The Ma distributions confirm that the numerical settings chosen for these simulations give rise to transonic flow conditions since, at the inlet, $Ma < 1$, then reaches values close $Ma = 1.5$ on the bump surface, and a shock restores subsonic conditions at the outlet of the domain.

Naturally, the resolution of the shock interface is greatly enhanced with the increase of grid density. The sharp discontinuity origins numerical oscillations at the back of the shock. However, those typically affect the same number of cells thus the region affected by these numerical oscillations tends to decrease with grid refinement. The same trends are also observed in [11].

The results for the grid convergence of T_o with the HARM and QUICK schemes follows the trends observed in figure 14. However, for the transonic conditions monotonically convergent solutions are computed for all schemes.

Considering the pressure, the solutions for the three schemes, CDS+0.1UP, HARM and QUICK, are similar in the finest grids. Despite the deviations of the UP solutions, all convective schemes estimate approximately the same exact solution.

3.4.3 Supersonic flow

Equivalent results to the previous two figures are shown in figure 16, but for the supersonic test case.

The flow, in fact, is fully supersonic, i.e. $Ma > 1$ throughout both walls, which validates changing the pressure imposition boundary condition to the inlet over the outlet of the domain (see sub-section 2.5).

Among the three undisturbed flow Mach number, the present one is the more demanding for the accu-

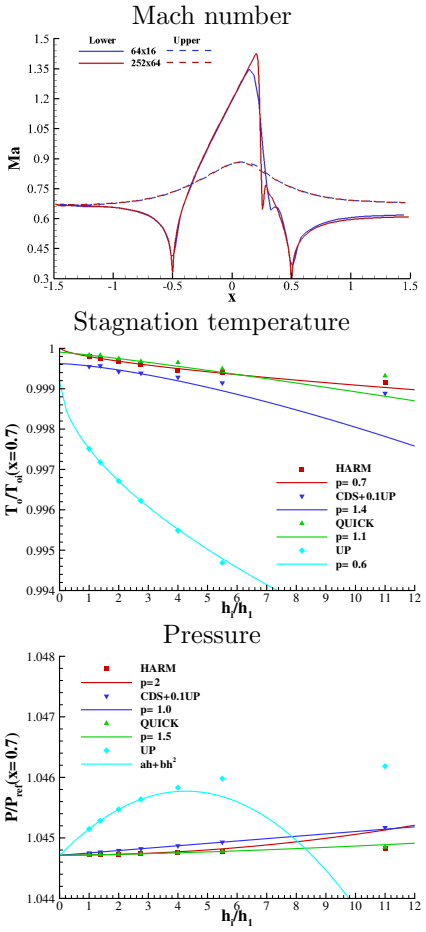

Figure 15: Mach distribution on the horizontal boundaries and grid convergence studies for stagnation temperature and pressure at $x = 0.55m$ on the lower wall. Two-dimensional transonic inviscid flow over a bump .

racy of the solution. Two oblique shocks are generated, at the leading and trailing edges of the bump, and the first is reflected on the top wall where the effect of grid coarsening is more negetivly felt. Moreover, numerical oscillation are present at the back of each shock. Like in the transonic conditions, those affect the same number of cells so in finest grids of this test case the anomalies are encompassed to a very small region of the domain. The same trends is ReFRESCO simulations are present in solutions found in [11].

In the supersonic conditions, none of the convection schemes converge with grid refinement to the expected solution of T_o, $T_o/T_{oi} = 1$. Not only that but, the estimate of the exact solution is different for every single scheme. Also, for this flow quantity, the the addition of extra fine grids (with $r_i < 1$) does not eliminate the solutions oscillatory behaviour.

Interestingly, there is still consistency in the extrapolated values for pressure. It should be mentioned that, the only forces acting of these flows are pressure forces. As a result, the consistency of pressure greatly benefits the convergence properties of the force coefficients.

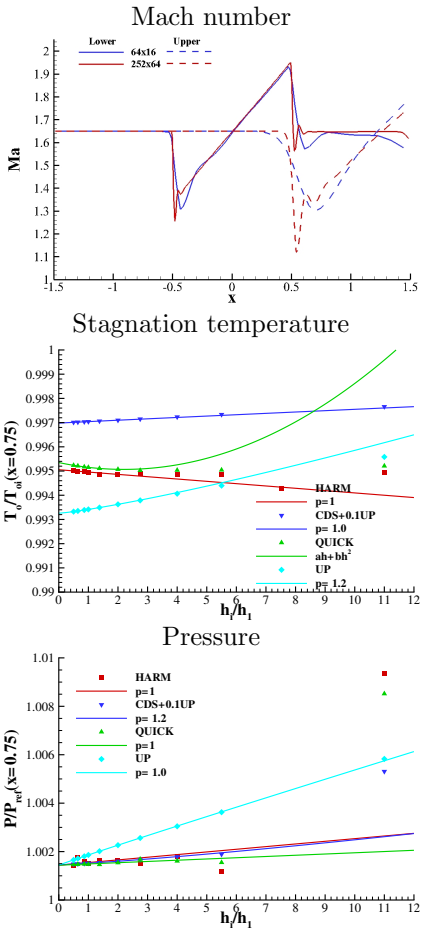

Figure 16: Mach distribution on the horizontal boundaries and grid convergence studies for stagnation temperature and pressure at $x = 0.55m$ on the lower wall. Two-dimensional supersonic inviscid flow over a bump .

4. Conclusions

In this article, a study of the robustness and accuracy of the single-phase, pressure-based, compressible flow solver in ReFRESCO, was performed. The iterative and discretization convergence properties were analysed in six different two-dimensional test cases, three viscous flow test cases taken from [14] and three cases featuring an inviscid flow, as seen in [2, 11]. Comparative data was taken from the previous sources to contrast with the solutions obtained by ReFRESCO.

The main conclusion to derive from the results of this work were:

- The compressible flow solver is robust as the residuals of the non-linear problem were converged to values close to machine accuracy,

from the 45 unique grids used, only in the sparsest grid of the NACA0012 an iteratively converged solution was not obtained.

- Extending the near-wall cell size at the solid surfaces to the wake region degrades the rate of convergence with the simulation time.

- Grid convergence properties are dependent on the convection scheme, inlet flow regime, quantity of interest and incoming flow angle of attack.

- Concerning the inviscid flow test case, estimations of the exact solution are not always consistent between the four convection schemes. This is mostly evidenced in the supersonic test case. The discrepancies are tied to the loss of stagnation temperature (that should remain constant) due to the geometric singularities and shocks. However, the pressure is consistent across all schemes.

- ReFRESCO yields consistent solutions in the two grid sets of the flat plate exercise, i.e. the error bars obtained for the two finest grids solutions intersect. Including the solutions from excessively sparse grids deteriorates the observed order of grid convergence. Insufficiently converged solutions of the non-linear problem leads to inconsistent estimations of the exact solution.

- The solutions obtained with ReFRESCO are in great graphical agreement with solutions from other CFD solvers, like CFL3D and FUN3D. However, some differences between the solutions of the three solvers are higher than the estimated numerical uncertainty of ReFRESCO. More definitive statements concerning the consistency of ReFRESCO are only possible if information regarding the uncertainty of the comparative data is available.

- Moreover, ReFRESCO accurately predicts solutions in subsonic, transonic and supersonic conditions, when comparing to other pressure-based solvers. However, oscillations can appear close to geometrical singularities and shocks.

References

[1] John David Anderson Jr. *Fundamentals of aerodynamics*. Tata McGraw-Hill Education, 2010.

[2] I. Demirdžić, ž Lilek, and M. Perić. A Collocated Finite Volume Method For Predicting Flows at All Speed. *Journal of Numerical Methods in Fluids*, 16(12):1029–1050, 1993.

[3] L. Eça and M. Hoekstra. A procedure for the estimation of the numerical uncertainty of CFD calculations based on grid refinement studies. *Journal of Computational Physics*, 262:104–130, 2014.

[4] N. Gregory and C. L. O'Reilly. Low-Speed Aerodynamic Characteristics of NACA 0012 Aerofoil Sections, including the Effects of Upper-Surface Roughness Simulation Hoar Frost. Technical Report 3726, NPL AERO, January 1970.

[5] L. Eça J. Muralha and C. Klaij. Application of the simple algorithm to a manufactured subsonic flow. In *21^{st} Numerical Towing Tank Symposium, NuTTS 2018*, 2018.

[6] L. Eça J. Muralha and C. Klaij. Assessing refresco compressible single phase flow solver numerical robustness. In *22^{nd} Numerical Towing Tank Symposium, NuTTS 2019*, 2019.

[7] K. C. Karki and S. V. Patankar. Pressure based calculation procedure for viscous flows at all speeds in arbitrary configurations. *AIAA Journal*, 27(9):1167–1174, 1989.

[8] C. L. Ladson, A. S. Hill, and W. G. Johnson, Jr. Pressure Distributions from High Reynolds Number Transonic Tests of an NACA 0012 Airfoil in the Langley 0.3-Meter Transonic Cryogenic Tunnel. Technical Report TM-100526, NASA, December 1987.

[9] Hoekstra M. *Numerical Simulation of Ship Stern Flows with a Space-Marching Navier-Stokes Method*. PhD thesis, University of Delft, 1999.

[10] Marin. Refresco, 2020.

[11] F. Moukalled and M. Darwish. A High-Resolution Pressure-Based Algorithm for Fluid Flow at All Speeds. *Journal of Computational Physics*, 168(1):101 – 130, 2001.

[12] F. Moukalled, L. Mangani, and M. Darwish. *The Finite Volume Method in Computational Fluid Dynamics An Advanced Introduction with OpenFOAM and Matlab*. Springer, 1 edition, 2016.

[13] S. V. Patankar and D. B. Spalding. A calculation procedure for heat, mass and momentum transfer in three-dimensional parabolic flows. *International Journal of Heat and Mass Transfer*, 15(10):1787–1806, 1972.

[14] Christopher Rumsey. NASA Langley Research Center Turbulence Modeling Resource, 2020.

[15] Allmaras S.R. Spalart P.R. A One-Equation Turbulence Model for Aerodynamic Flows. In *AIAA 30^{th} Aerospace Sciences Meeting, Reno, U.S.A.*, 1992.

[16] Jiyuan Tu, Guan Heng Yeoh, and Chaoqun Liu. *Computational fluid dynamics: a practical approach*. Butterworth-Heinemann, 2018.

[17] Waterson, Nicholas P. and Deconinck, Herman. Design Principles for Bounded Higher-Order Convection Schemes–a Unified Approach. *Journal of Computational Physics*, 224(1):182–207, 2007.

[18] David C. Wilcox. *Turbulence Modeling for CFD*. DCW Industries, 3rd edition, 2006.